GND-RI: A Normalized Difference Form More Suitable for Remote Sensing Applications

Linxin Zou and Bo Wei

***Abstract*— The normalized difference index (NDI) originates from NDVI, which has been widely used in remote sensing applications and to guide the development of NDI in other fields due to its excellent performance; however, injective mapping from the original bands to NDI leads to information loss in land cover classification. When NDI is represented as a simple form, it is, furthermore, prone to premature saturation in specific change detection and variable inversion tasks. In this study, we first propose the radius index (RI), a new index to represent illumination variations by using the missing band information from NDI. Based on RI, we develop a generalized NDI (GND) by adding four positive scaling coefficients to NDI foundation, and the value range and sensitivity of GND are adjusted by these four coefficients, which are derived from the statistical information of the study area. The derivation of these four coefficients is, moreover, reversible, making it possible to interpret the applicable range of the derived set of coefficients. Our experiments demonstrate that: 1) GND is more effective in terms of improving saturation than the traditional indices and 2) mapping the original bands to GND-RI (GND combined with RI) can guide classifiers to learn more generalized features based on spectral information and thus achieve higher classification accuracy both in machine learning and the latest deep learning semantic segmentation models. The data and code for the article can be found at https://github.com/Zoulinx/GND.**

***Index Terms*— Feature classification, feature mapping, normalized difference index (NDI), sensitivity function, spectral index.**

I. Introduction

THE spectral index is the most commonly used index to analyze data in optical remote sensing [1]. Generally, the spectral index within the solar spectral range is a combination of the spectral reflectance of two or more spectral bands, which can indicate the reflective spectral characteristics of various objects interacting with solar radiation. The spectral index is a more relevant feature to the research target compared to the original spectral band reflectance. The usage of appropriate spectral indices may, therefore, make achieving remote sensing objectives easier and more efficient [2].

The normalized difference index (NDI) is the most popular way to combine bands in the spectral index. NDVI [3] is the first spectral index constructed by the normalized difference approach and is the most popular vegetation index thus far [4]. Statistically, there are tens of thousands of papers on NDVI [5]. These papers cover various remote sensing applications, such as feature classification [6], change monitoring [7], [8], and biophysical volume inversion [9], [10]. The success of NDVI has led to the promotion of normalized difference forms in the field of spectral feature extraction and the development of a series of spectral indices of dominant features in their respective fields.

For instance, the normalized burn ratio (NBR) [11] and its improved form, the dNBR [12], are commonly used for monitoring vegetation burns. The normalized difference water index (NDWI) [13] and its improved version MNDWI [14], are employed for water extraction. Additionally, the normalized difference building index (NDBI) [15] and the normalized difference snow index (NDSI) [16] are used for building and snow extraction, respectively.

The popularity of NDI is generally due to the following three reasons.

1) The band selection strategy of NDI is to find a group of high-contrast bands with higher and lower reflectances for the initial target compared to other targets, which can strongly highlight the reflectance characteristics of the initial target.
2) NDI does not contain any constant terms, and the form of the pure band ratio can weaken the influences of topographic effects on the illumination difference [17], [18].
3) NDI has a convergent and symmetric value range $[-1, 1]$.

In fact, the simple ratio index (SR) possesses the same advantages as NDI except for the convergent value range. NDI can be rewritten as a function of SR with SR as the only independent variable [19]:

$$\mathrm{NDI} = f(\mathrm{SR}) = \frac{\mathrm{SR} - 1}{\mathrm{SR} + 1}. \tag{1}$$

From this perspective, most of the advantages of NDI are inherited from SR, and its improvement lies in the scaling of the SR value range; however, this scaling comes at a cost; SR has an infinite divergence value range and is not initially a

Manuscript received 25 August 2022; revised 7 May 2023 and 25 July 2023; accepted 26 July 2023. Date of publication 1 August 2023; date of current version 16 August 2023. This work was supported in part by the National Natural Science Foundation of China under Grant 41461085, in part by the BaGui Scholars Special Funds of Guangxi Province under Grant 2019-79, in part by the Foundation of Guangxi Key Laboratory of Spatial Information and Geomatics under Grant 16-380-25-04, and in part by the Doctoral Foundation of Guilin University of Technology under Grant 1996015. *(Corresponding author: Bo Wei.)*

Linxin Zou is with the College of Geomatics and Geoinformation, Guilin University of Technology, Guilin 541004, China (e-mail: linxinzou@foxmail.com).

Bo Wei is with the College of Geomatics and Geoinformation, Guilin University of Technology, Guilin 541004, China, and also with the Guangxi University Key Laboratory of Ecological Spatiotemporal Big Data Perception Service, Guilin University of Technology, Guilin 541004, China (e-mail: superweibo@glut.edu.cn).

Digital Object Identifier 10.1109/TGRS.2023.3300834

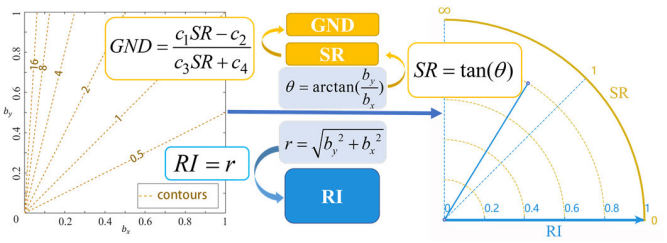

Fig. 1. Coordinate system representation of features. (Left) Cartesian coordinate system representation of the feature band group (b_x, b_y). (Right) Polar coordinate system representation of SR and RI.

saturated function but becomes saturated after being scaled by NDI [20].

A series of NDI-based scaling schemes have been proposed in past studies, such as the angular vegetation index (AVI) that uses an inverse tangent function [6], MNDVI [21], and WDRVI [22], which adds a constant coefficient, NDVIv multiplied by near-infrared reflectance [23], and KNDVI that uses the tanh function [24]; however, there are three problems in the above schemes.

1) NDI is a function with SR as an independent variable, and scaling NDI is equivalent to indirectly scaling SR. In contrast, directly scaling SR more closely resembles the essence of the problem than scaling NDI.
2) The mapping from the feature bands to NDI involves information loss.
3) The spectral indices with the coefficients derived from the statistical information of the study area can modify the sensitivity of NDI (for example, MNDVI and WDRVI as the improvements to NDVI), but the derivation of these coefficients is irreversible, meaning that it is difficult to infer the applicable range from the derived coefficients themselves.

In this study, we propose the generalized NDI (GND) and radius index (RI) to address the above issues. GND-RI (GND combined with RI) form a bijection with the original feature bands (b_x, b_y), inspired by the mapping from Cartesian coordinates to polar coordinates. As shown in Fig. 1, (b_x, b_y) are first mapped to the polar angle and radius (θ, r), where SR is the tangent of θ. GND is a scaled version of SR, with its range and sensitivity to changes in SR adjusted by four positive scaling coefficients c_1, c_2, c_3, and c_4, and RI corresponds directly to r, representing the information lost in SR.

The rest of this study is organized as follows. In Section II, we provide a detailed demonstration of the derivation process for RI and GND. In Section III, we demonstrate how to use GND to address the saturation of NDVI in vegetation cover changes and compare it with other vegetation indices. Section IV presents the impact on classifications after mapping the original bands to GND-RI. Some discussions are conducted in Section V, and the entire study is concluded in Section VI.

II. Proposed Generalized Normalized Difference Index

In this section, we study the complete mapping process from the most primitive feature bands to NDI. Because SR and NDI are both multivariate functions with two feature bands as two independent variables, the scaling process of the feature bands to NDI can be described as follows. Let b_x and b_y be two feature bands, and the scatter (b_x, b_y) be the feature band group in spectral space. Thus, SR maps (b_x, b_y) to a single-valued output in the interval $[0, +\infty)$, and then NDI maps SR to a single-valued output in the interval $[-1, 1]$:

$$(b_x, b_y) \rightarrow \text{SR} \rightarrow \text{NDI}. \tag{2}$$

In (2), SR to NDI is a bijection with no information loss, but the mapping of (b_x, b_y) to SR is injective with information loss, and SR cannot respond to the changes of the scatter completely (e.g., SR does not respond to equal scale increases of the feature band); therefore, neither SR nor NDI can completely describe the changes in (b_x, b_y). To complement the lost information in SR, a new mapping needs to be added to SR to make it a bijection for b_x and b_y:

$$f(b_x, b_y) = \sqrt{b_x^2 + b_y^2}. \tag{3}$$

The mapping $f(b_x, b_y)$ is equivalent to the distance from the points in the b_x and b_y feature space to the origin. Considering that SR can weaken the influence of the illumination differences caused by the topographic effect and $f(b_x, b_y)$ can be regarded as a supplement to the illumination information, we define $f(b_x, b_y)$ as an illumination change index, i.e., RI:

$$\text{RI} = \sqrt{b_x^2 + b_y^2}. \tag{4}$$

The mappings of $f(b_x, b_y)$ after adding RI are expressed as:

$$\begin{aligned} (b_x, b_y) &\rightarrow \text{SR} \\ (b_x, b_y) &\rightarrow \text{RI}. \end{aligned} \tag{5}$$

According to Fig. 1, the inverse mappings of b_x and b_y to SR and RI are described as:

$$\begin{aligned} b_x &= \text{RI}\cos(\arctan(\text{SR})) \\ b_y &= \text{RI}\sin(\arctan(\text{SR})). \end{aligned} \tag{6}$$

According to the nature of bijection, any changes in the scatter (b_x, b_y) can be decomposed into components in SR and RI directions, which means that the necessary and sufficient condition for SR to be sensitive to a change is that the change has a large component in the SR direction; therefore, in the following discussion of function sensitivity, only changes in SR component are of interest, and RI is considered a constant.

The sensitivity of SR to changes in (b_x, b_y) is discussed first. Since the change direction of (b_x, b_y) is arbitrary, only the most sensitive gradient direction is discussed. The gradient of SR with respect to (b_x, b_y) can be expressed as:

$$\nabla \text{SR}(b_x, b_y) = \left\{ \frac{\partial \text{SR}}{\partial b_x}, \frac{\partial \text{SR}}{\partial b_y} \right\} = \left(-\frac{b_y}{b_x^2}\vec{i}, \frac{1}{b_x}\vec{j} \right). \tag{7}$$

The sensitivity in this direction is expressed using the modulus of the gradient:

$$\left\| \nabla \text{SR}(b_x, b_y) \right\| = \frac{\sqrt{b_x^2 + b_y^2}}{b_x^2} = \frac{1 + \text{SR}^2}{\text{RI}}. \tag{8}$$

According to (8), the maximum sensitivity of SR to changes in (b_x, b_y) is proportional to the square of SR corresponding to the point (b_x, b_y), and the saturation point of the function is at SR $= 0$. This conclusion is consistent with the application

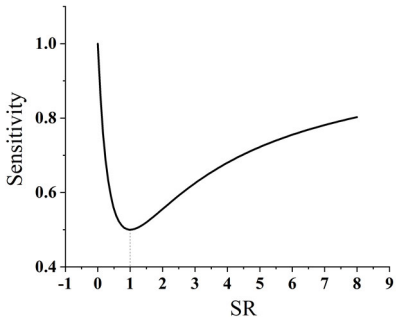

Fig. 2. Sensitivity of NDI versus SR, where the sensitivity is replaced by the modulus of the gradient.

results of the ratio vegetation index (RVI): RVI is insensitive to changes in low vegetation cover (small SR) and sensitive to changes in high vegetation cover (high SR). Second, the sensitivity of NDI to changes in (b_x, b_y) is discussed using the same approach. The gradient of NDI with respect to (b_x, b_y) is expressed as follows:

$$\nabla \mathrm{NDI}(b_x, b_y) = \left(-\frac{2b_y}{(b_x + b_y)^2} \vec{i}, \frac{2b_x}{(b_x + b_y)^2} \vec{j} \right). \quad (9)$$

Correspondingly, the modulus of the gradient of NDI is expressed as:

$$\left\| \nabla \mathrm{NDI}(b_x, b_y) \right\| = \frac{(1 + \mathrm{SR}^2)}{(1 + \mathrm{SR})^2} \cdot \frac{2}{\mathrm{RI}}. \quad (10)$$

According to (10), the maximum sensitivity of NDI to changes in (b_x, b_y) is no longer monotonically related to SR. To illustrate the functional relationship more intuitively, RI in (10) is set as a constant value of 1, and the figure of the modulus of the gradient as a function of SR is plotted, as shown in Fig. 2.

It can be seen from Fig. 2 that with an increase in SR, the maximum sensitivity of SR to changes in (b_x, b_y) first decreases and then increases, and the minimum point occurs when SR = 1. This conclusion implies that the saturation point for the changes in (b_x, b_y) shifts from SR = 0 to SR = 1 after SR scaling to NDI. This shift of the saturation point is very important for the design of the spectral index because we want the spectral index to be sensitive to changes of interest and saturated with changes of disinterest, and this can be achieved by adjusting the position of the saturation point exactly. For example, because NDVI is sensitive to changes in low vegetation cover and insensitive to changes in high vegetation cover, the saturation point can be adjusted to a region away from high vegetation cover if we want to increase its sensitivity to changes in high vegetation cover.

To investigate the effect of the scaling of NDI to SR on the position of the saturation point, we propose a parametric form of NDI, namely, GND:

$$\mathrm{GND} = \frac{c_1 \mathrm{SR} - c_2}{c_3 \mathrm{SR} + c_4} \quad (11)$$

where c_1, c_2, c_3, and c_4 are the four positive coefficients. The gradient of GND with respect to (b_x, b_y) is expressed as:

$$\nabla \mathrm{GND}(b_x, b_y) = \left(-\frac{(c_2 c_3 + c_1 c_4) b_y}{(c_3 b_y + c_4 b_x)^2} \vec{i}, \frac{(c_2 c_3 + c_1 c_4) b_x}{(c_3 b_y + c_4 b_x)^2} \vec{j} \right). \quad (12)$$

Correspondingly, the modulus of the gradient of GND is expressed as:

$$\| \nabla \mathrm{GND}(bx, by) \| = \frac{(c_2 c_3 + c_1 c_4)}{\left(c_3^2 + \frac{c_4^2 + 2 c_3 c_4 \mathrm{SR} - c_3^2}{1 + \mathrm{SR}^2} \right) * \mathrm{RI}}. \quad (13)$$

To simplify the analysis, the part of (13) containing SR is denoted by $f(\mathrm{SR})$:

$$f(\mathrm{SR}) = \frac{c_4^2 + 2 c_3 c_4 \mathrm{SR} - c_3^2}{1 + \mathrm{SR}^2}. \quad (14)$$

Accordingly, (12) can be expressed as:

$$\| \nabla \mathrm{GND}(bx, by) \| = \frac{(c_2 c_3 + c_1 c_4)}{(c_3^2 + f(\mathrm{SR}))\mathrm{RI}}. \quad (15)$$

According to (14), the sensitivity of GND to changes in (b_x, b_y) is inversely proportional to $f(\mathrm{SR})$, and further derivation of $f(\mathrm{SR})$ with respect to SR can be described as:

$$\frac{df(\mathrm{SR})}{\mathrm{dSR}} = \frac{-2 c_3 c_4 \mathrm{SR}^2 + 2(c_4^2 - c_3^2)\mathrm{SR} + 2 c_3 c_4)}{(\mathrm{SR}^2 + 1)^2}. \quad (16)$$

In (16), the denominator is a constant positive, and the numerator is a downward opening parabola. When SR increases, the changes in GND sensitivity are divided into three procedures.

1) The derivative function is positive when SR belongs to the interval $(0, c_3/c_4)$, and the sensitivity of GND decreases when the value of $f(\mathrm{SR})$ increases.
2) The derivative function is zero when $\mathrm{SR} = c_3/c_4$. At this time, $f(\mathrm{SR})$ takes the maximum value, and the sensitivity of GND reaches the minimum; that is, it is at the most saturated state.
3) The derivative function is negative when SR belongs to the interval $(c_3/c_4, +\infty)$, and the sensitivity of GND gradually increases when the value of $f(\mathrm{SR})$ decreases.

An important conclusion can be drawn from the above process; that is, the saturation point of GND can be arbitrarily moved along the interval $[0, +\infty]$ by adjusting the ratio of coefficients c_3 and c_4. In particular, as mentioned above, the saturation point of NDI is located at SR = 1 because NDI corresponds to the special case, where GND takes $c_3 = 1$ and $c_4 = 1$.

We observe that the sensitivity of GND to the region of interest, however, does not continually increase when the saturation point is located far away from the region of interest. In fact, it shows an initial increase followed by a decrease. For example, with a step of 0.1 and the value range unchanged, SR = 5 is selected as the area of high vegetation cover, and the scaling coefficients are adjusted to move the NDVI saturation point from SR = 1 to SR = 0. Then, we set RI to a constant of 1 and calculate the sensitivity of NDVI to SR = 5 at each movement, and the results can be obtained, as shown in Fig. 3.

From Fig. 3, it can be seen that the sensitivity is the extreme value, i.e., SR = 0.2, when the saturation point is moved. The next question is, therefore, how to calculate the location of the extreme value; furthermore, we need to know whether there exists a group of scaling coefficients that ensure the maximum sensitivity of GND with respect to the specified point (b_x, b_y) in the spectral space.

After derivation, it is found that if the range of GND is symmetric about the origin, i.e., the four scaling coefficients

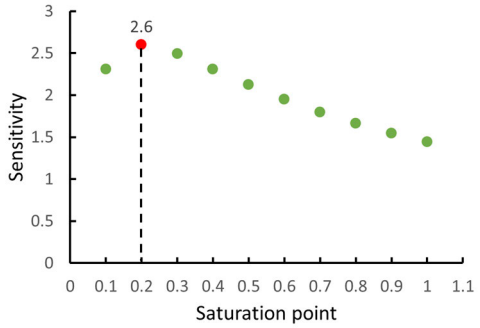

Fig. 3. Relationship between the saturation point location and NDVI sensitivity, where the sensitivity is replaced by the modulus of the gradient.

satisfy $c_1 = c_3$ and $c_2 = c_4$. Then, the modulus of the gradient of GND can be expressed as:

$$\left\|\nabla \mathrm{GND}(b_x, b_y)\right\| = \frac{2c_3c_4}{\left(c_3^2 + \frac{c_4^2+2c_3c_4\mathrm{SR}-c_3^2}{1+\mathrm{SR}^2}\right)\mathrm{RI}}. \tag{17}$$

To simplify the analysis, let $f(c_3, c_4) = c_4/c_3$ and substitute it into (17):

$$\left\|\nabla \mathrm{GND}(b_x, b_y)\right\| = \frac{2\left(1+\mathrm{SR}^2\right)}{\mathrm{RI}} \times \frac{f(c_3, c_4)}{(\mathrm{SR} + f(c_3, c_4))^2}. \tag{18}$$

Taking the partial derivative of $f(c_3, c_4)$ in (18) yields:

$$\frac{\partial}{\partial f(c_3, c_4)} \parallel \nabla \mathrm{GND}(b_x, b_y) \parallel = \frac{2\left(1+\mathrm{SR}^2\right)}{\mathrm{RI}(\mathrm{SR} + f(c_3, c_4))^3} \cdot (\mathrm{SR} - f(c_3, c_4)). \tag{19}$$

In (19), the result to the left side of the multiplication sign is a constant positive, and to the right, it is a straight line with a negative slope. When $f(c_3, c_4)$ increases, the changes in sensitivity of GND are divided into three conditions.

1) The derivative function is positive when $f(c_3, c_4)$ belongs to the interval (0, SR), and the sensitivity of GND increases gradually.
2) The derivative function is zero when $f(c_3, c_4) = \mathrm{SR}$, and the sensitivity of GND reaches its maximum value.
3) The derivative function is negative when $f(c_3, c_4)$ falls within the interval (SR, $+\infty$), and the sensitivity of GND decreases gradually.

The above condition demonstrates that when the range of GND is symmetric about the origin, there exists a group of scaling coefficients that force the sensitivity of GND to have an extreme value with respect to the specified point (b_x, b_y) in the spectral space, in which the extreme point is determined by the ratio of the coefficients c_4 and c_3.

In summary, we provide a complete explanation of GND and RI, that is, (GND, RI) is the reversible mapping of the feature bands (b_x, b_y), which is similar to the mapping of RGB to HSI and aims to decompose the original feature band information into spectral feature information and the illumination difference. GND represents the spectral feature information in (GND, RI), and its expression is as follows:

$$\mathrm{GND} = \frac{c_1b_y - c_2b_x}{c_3b_y + c_4b_x} \tag{20}$$

where c_1, c_2, c_3, and c_4 are four positive scaling coefficients, which determine the value range of GND together:

$$\mathrm{GND} \in \left[-\frac{c_2}{c_4}, \frac{c_1}{c_3}\right]. \tag{21}$$

As a complement to GND, RI represents the difference in illumination in (GND, RI), and the contours of RI and GND are orthogonal everywhere.

Assuming that RI is constant, GND possesses two important properties.

1) Given a group of definite scaling coefficients, there exists a saturation point for the maximum sensitivity of GND to changes in (b_x, b_y), and the saturation point (b_x, b_y) satisfies:
$$\frac{b_y}{b_x} = \frac{c_3}{c_4}. \tag{22}$$
2) When the value range of GND is symmetric about the origin, given any point (b_x, b_y) in the feature band space, there exists a group of scaling coefficients for which the maximum sensitivity of GND to the change of the point (b_x, b_y) is maximized, and the relationship between the scaling coefficients and the point (b_x, b_y) is expressed as:
$$\frac{c_4}{c_3} = \frac{b_y}{b_x}. \tag{23}$$

In this study, we refer to the ratio of the coefficients c_4 to c_3 as the sensitive point of GND.

III. Enhancing NDVI With GND

In this section, we use the leaf area index (LAI) as a proxy for vegetation coverage and assess the sensitivity of indices to vegetation changes based on the linear regression results between the indices and LAI values. Similar to NDVI, the red and near-infrared bands are set as the feature bands for GND. We demonstrate how GND addresses the saturation of NDVI at high vegetation cover changes and how to select the optimal coefficients for GND based on the study area. It is worth noting that these improvements in GND are not limited to the vegetation index.

A. Study Area

The study area is the Longkang farm site in Anhui Province, China, for which there is the ValLAI_Crop open dataset. Compared with other sites using Landsat 5 satellite images before 2007, this site uses the latest data collection time (in 2017) and available satellite images (Landsat 8 images) [25].

In our experiments, the data in the study area are processed as follows.

1) Four sample plots from March 26, 2017, are discarded due to excessive cloud cover.
2) The raster drivers of the original data are corrected by converting from GTiff (.tif) to ENVI (.dat).
3) The sample plots are supplemented with corresponding Landsat 8 Collection 2 data.

As shown in Fig. 4, the four sample plots Point1, Point3, Point8, and Point15 with different vegetation coverage levels on April 23, 2017, are used as our experimental data. According to [25], the average LAIs of these four sample plots are 4.055, 4.457, 2.665, and 3.200, respectively.

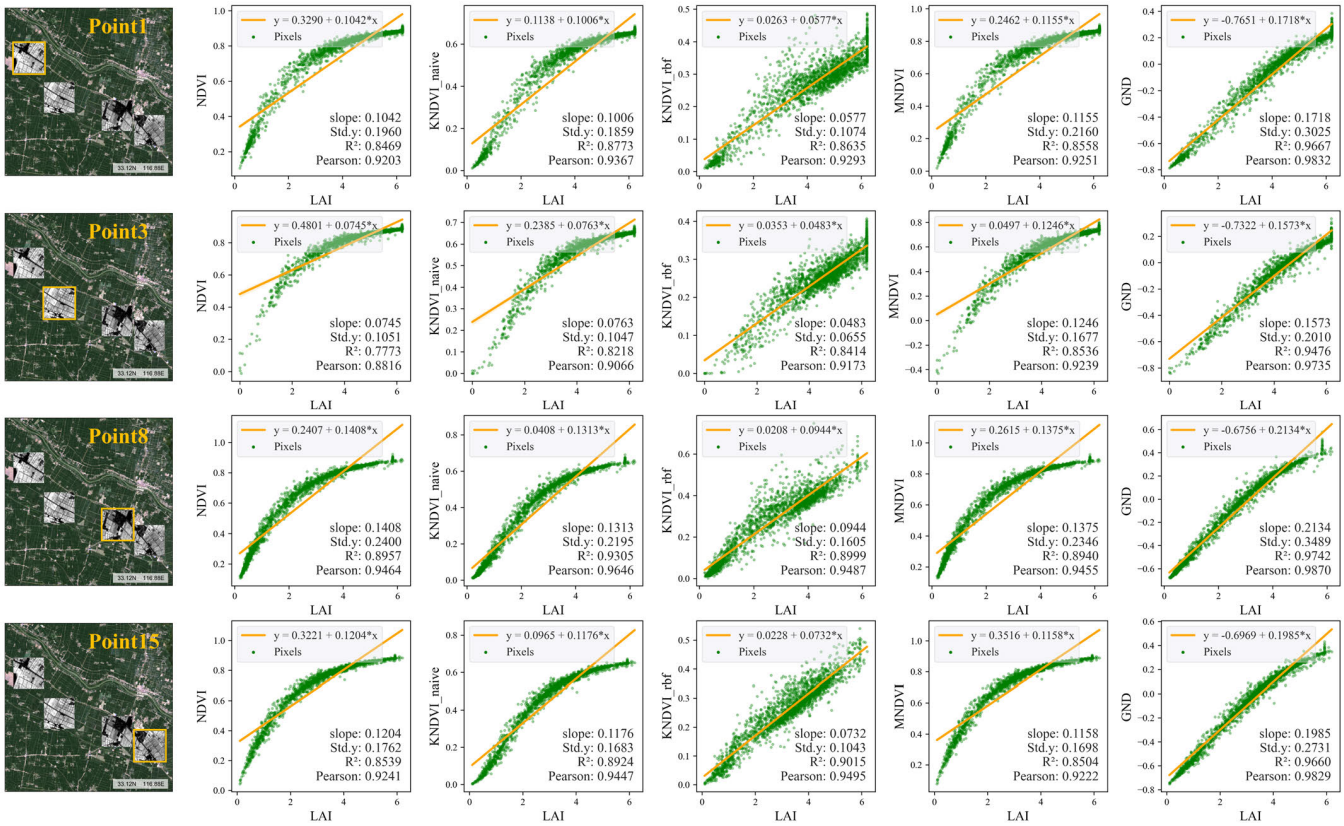

Fig. 4. Linear regression results of NDVI, KNDVI, MNDVI, and GND with LAI in four sample plots.

B. Vegetation Indices

To illustrate the performance of GND in the vegetation index, we compare GND with NDVI, MNDVI, and KNDVI, in which the last two indices are the vegetation indices with adaptive coefficients.

NDVI is the baseline of the vegetation index and is expressed as:

$$\mathrm{NDVI} = \frac{\rho_{\mathrm{NIR}} - \rho_{\mathrm{red}}}{\rho_{\mathrm{NIR}} + \rho_{\mathrm{red}}} \tag{24}$$

where ρ_{NIR} is the near-infrared reflectance and ρ_{red} is the red reflectance.

MNDVI improves the sensitivity of NDVI by adding a positive coefficient c to NDVI:

$$\mathrm{MNDVI} = \frac{c\rho_{\mathrm{NIR}} - \rho_{\mathrm{red}}}{c\rho_{\mathrm{NIR}} + \rho_{\mathrm{red}}} \tag{25}$$

where c is determined by the standard deviation of the near-infrared band σ_{NIR} and red band σ_{red} in the study area and is calculated as follows:

$$c = \sqrt{\frac{\sigma_{\mathrm{red}}^2}{\sigma_{\mathrm{NIR}}^2}}. \tag{26}$$

KNDVI improves NDVI by using kernel methods, especially adopting the RBF kernel, considering the higher-order correlation between near-infrared and red bands:

$$\mathrm{KNDVI}_{\_\mathrm{rbf}} = \tanh\left(\left(\frac{\rho_{\mathrm{NIR}} - \rho_{\mathrm{red}}}{2\sigma}\right)^2\right) \tag{27}$$

where σ is estimated from the region or biome through the average distance between all N pixels therein:

$$\sigma = \frac{\sum_i^N |\rho_{\mathrm{NIR}_i} - \rho_{\mathrm{red}_i}|}{N}. \tag{28}$$

KNDVI, moreover, has a naive version that simplifies σ as the mean value of the near-infrared and red bands for each pixel. In this case, KNDVI can be considered as a function with NDVI as the unique independent variable:

$$\mathrm{KNDVI}_{\_\mathrm{naive}} = \tanh\left(\mathrm{NDVI}^2\right). \tag{29}$$

Assuming the value range of GND is $[-1, 1]$, which is the same as that of NDVI and MNDVI, the coefficient c_2 should be equal to the coefficient c_4, and the coefficient c_1 should be equal to the coefficient c_3 according to (21):

$$\mathrm{GND} = \frac{c_3\rho_{\mathrm{NIR}} - c_4\rho_{\mathrm{RED}}}{c_3\rho_{\mathrm{NIR}} + c_4\rho_{\mathrm{RED}}} = \frac{\rho_{\mathrm{NIR}} - \frac{c_4}{c_3}\rho_{\mathrm{RED}}}{\rho_{\mathrm{NIR}} + \frac{c_4}{c_3}\rho_{\mathrm{RED}}}. \tag{30}$$

In this case, GND is most sensitive to vegetation changes when the ratio of the near-infrared band to the red band (i.e., SR) is equal to that of c_4 to c_3, according to (23). Otherwise, the ratio of c_4 to c_3 should be equal to the SR of most vegetation in the study area to make GND sensitive to changes in vegetation coverage.

In this study, the maximum likelihood estimation method is used to estimate the normal distribution of SR, and the mean value of the normal distribution is used as a proxy for the SR of most vegetation in the study area. Because the analytical solution for the mean of a normal distribution is equivalent to

TABLE I
COEFFICIENTS OF THE VEGETATION INDICES EXTRACTED FROM THE STUDY AREA

c in MNDVI	σ in KNDVI	c_4/c_3 in GND
	Point1	
0.8374	0.3155	10.3998
	Point3	
0.4070	0.3315	11.3871
	Point8	
1.0436	0.2441	6.5362
	Point15	
1.0663	0.2774	7.7431

the sample mean, the ratio of c_4 to c_3 can be estimated as:

$$\frac{c_4}{c_3} = \frac{\sum_i^N \frac{\rho_{\mathrm{NIR}_i}}{\rho_{\mathrm{red}_i}}}{N}. \tag{31}$$

Based on the statistical information obtained by (26), (28), and (31) of the four sample plots in the study area, the corresponding coefficients for MNDVI, KNDVI, and GND are calculated, and their results are shown in Table I.

C. Results and Discussion

As shown in Fig. 4, GND exhibits the highest correlation (Pearson) and goodness of fit (R^2) with LAI compared with those of NDVI, KNDVI, and MNDVI for every sample plot. For Point 3, the Pearson and R^2 of GND are 0.0919 and 0.1703 higher than those of NDVI, respectively, with the highest average LAI.

GND inevitably exhibits negative values for some vegetation categories, but it is also beneficial. For example, assuming NDVI $>$ 0.3 is used to distinguish between vegetation and nonvegetation, the response range for nonvegetation changes is $[-1, 0.3]$, while the response range for vegetation changes is $(0.3, 1]$. Clearly, the response range for vegetation changes in the value range of NDVI is smaller than that for nonvegetation changes.

This problem can, however, be solved by GND. Point 1 is selected as an example. The expression of GND based on Table I and (30) is as follows:

$$\mathrm{GND} = \frac{\mathrm{SR} - 10.3998}{\mathrm{SR} + 10.3998}. \tag{32}$$

According to (1), an NDVI $>$ 0.3 is equivalent to an SR $>$ 1.86. By substituting SR $>$ 1.86 into (32), we can obtain the decision boundary for GND at a GND $>$ -0.7, which means that the response range for nonvegetation changes is $[-1, -0.7]$, while the response range for vegetation changes is $(-0.7, 1]$. Compared with the response range for vegetation changes, which accounts for 35% of the value range of NDVI, the response range can reach 85% with GND; therefore, GND is more suitable for index-based change detection algorithms, such as LandTrendr [7].

In contrast, the KNDVI loses the decision boundary for vegetation extraction because the characteristic of higher near-infrared reflectance than red reflectance in vegetation is eliminated due to the squaring operation of the KNDVI.

Although NDVI, MNDVI, and GND all share the same value range and can retain the decision boundary for vegetation extraction, their differences in sensitivity can still be found by observing the standard deviation (Std.y) and the linear regression coefficient (slope).

As shown in Fig. 4, GND has a higher Std.y and slope than those of NDVI and MNDVI, which implies that GND can allocate more value ranges to represent vegetation coverage changes while compressing the representation of nonvegetation changes within smaller value ranges.

IV. GENERALIZATION CAPABILITY OF GND-RI

In the previous derivation, RI is constructed to represent illumination difference information. In this section, we investigate the generalizability of the classification models in terms of handling illumination variations after mapping the original bands to GND-RI.

Remote sensing images become surface reflectance data with physical significance after various preprocessing steps, such as radiometric calibration, atmospheric correction, and orthorectification. Theoretically, reflectance data are more generalizable than ordinary color images in classification tasks; however, the reflectance data of the solar spectrum still have illumination difference errors caused by topographic effects, cloud shadows, object geometry, etc., which cannot currently be eliminated in the preprocessing steps. It is beneficial, therefore, to improve the classification accuracy by enhancing the generalization of the classification model in the illumination difference region.

Common algorithms for feature classification can be divided into two categories: machine learning algorithms based on the spectral domain and deep learning algorithms based on the spectral-space domain. This study, therefore, discusses the above two algorithms.

In the following experiments, a feature band group and an index group are designed for comparison. The input features of the index group include the normalized difference indices, NDBI, NDWI, and NDVI, which are combined with RI. The input features of the feature band group are those original feature bands corresponding to the index group. As discussed in Section III, the decision boundaries of GND and NDI can be converted to each other; therefore, it is required to select coefficients for GND in the index group only to maintain consistency with the form of NDI, as shown in Table II.

A. Spectral Domain Classification

The support vector machine (SVM) [27], [28] and random forest (RF) [29], [30] algorithms are selected for the experiments. These algorithms are representative of the spectral domain classification models. Since the above algorithms only consider spectral information, the classification results can be used to infer the spectral features learned by the classification models to explain the influences of GND-RI on the feature learning of the classification models.

1) *Study area:* The study area is Guilin city, China, which is situated upon a karst landscape and has a diverse natural environment and complex topography. In this region, karst is distributed over 96% of the landscape. Because of the complex karst topography, there are large illumination differences in

TABLE II
INPUT FEATURES OF THE TWO EXPERIMENTAL GROUPS

Feature band group	Index group
	Water
○B3	● $NDWI = \frac{B3-B7}{B3+B7}$
○B7	● $RI_{water} = \sqrt{B3^2 + B7^2}$
	Vegetation
○B4	● $NDVI = \frac{B8-B4}{B8+B4}$
○B8	● $RI_{veg} = \sqrt{B4^2 + B8^2}$
	Building
○B8A	● $NDBI = \frac{B11-B8A}{B11+B8A}$
○B11	● $RI_{building} = \sqrt{B8A^2 + B11^2}$

TABLE III
PARAMETERS USED IN THE SVM AND RF ALGORITHMS

Hyperparameters	Value
SVM	
Kernel Type	RBF
Gamma	1/6
RF	
N_estimators	100
Max_features	Square Root
Criterion	Gini coefficient

Guilin satellite images, which makes the location beneficial to test the generalizability of the GND-RI decomposition method to illumination differences.

2) *Data sources:* Using the surface reflectance data of Sentinel2 L2A provided by the USGS, the aerosol band B1, water vapor band B9, and cirrus band B10, each with a resolution of 60 m, are removed, and the remaining bands are resampled to a resolution of 10 m using the CN algorithm [31], [32].

3) *Samples:* Building, water, and vegetation are selected as the study objects. To test the generalizability of the model, only 64-pixel points of each class object are selected as training samples.

The specific parameters of the SVM and RF algorithms are shown in Table III. The kernel is the radial basis function (RBF) [33], and the hyperparameters of the kernel function are the reciprocal 1/6 of the number of input features [34] in the SVM algorithm. In the RF algorithm, the Gini coefficient is the metric, Max_features refers to the square of the number of features, and the integration scale is 100. The final obtained classification results are shown in Fig. 5.

We analyze the SVM classification results of both groups first, and some of the water extraction results of the SVM are shown in Fig. 6. From these figures, it can be seen that the main difference between the extraction results from the two

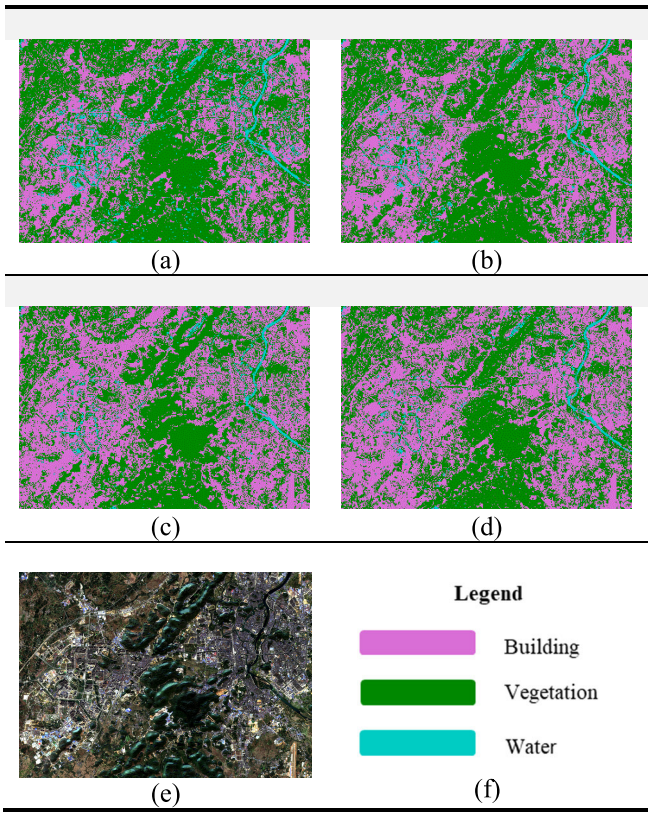

Fig. 5. Classification results of the two experimental groups. (a) Feature band group with the SVM. (b) Index group with the SVM. (c) Feature band group with the RF. (d) Index group with the RF. (e) Original image. (f) Legend.

Fig. 6. Water extraction results of the two experimental groups with the SVM. (a) Original image. (b) Feature band group. (c) Index group.

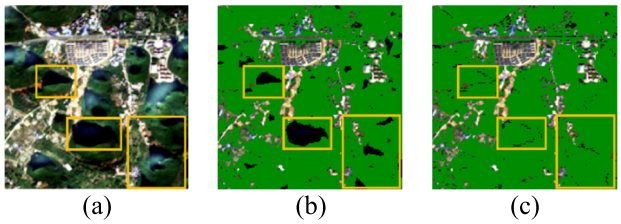

Fig. 7. Vegetation extraction results of the two experimental groups with the SVM. (a) Original image. (b) Feature band group. (c) Index group.

groups is that only a few shadows are identified as water by the SVM for the index group, while all the building shadows with generally low reflectivity are identified as water by the SVM in the feature band group because the identification of features of water with generally low reflectivity have also been learned by the SVM.

The partial vegetation extraction results of the SVM are, moreover, shown in Fig. 7. Similarly, the vegetation areas in

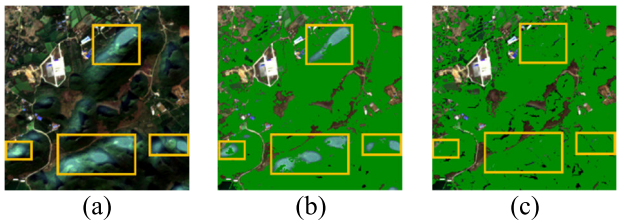

Fig. 8. Vegetation extraction results of the two experimental groups with the RF. (a) Original image. (b) Feature band group. (c) Index group.

shadow occlusion are correctly identified by the SVM in the index group, while they cannot be correctly identified by the SVM in the feature band group.

Second, the RF classification results of both groups were analyzed. The partial vegetation extraction results of the RF are shown in Fig. 8. Contrary to the SVM, the overly illuminated vegetation areas are correctly identified by the RF in the index group, while they cannot be correctly identified by the RF in the feature band group.

In summary, in the machine learning algorithms based on spectral domain classification, the differences between the two groups of classification results are mainly concentrated in the areas with illumination differences. With the same amount of information, better classification results are obtained with the index group in these areas, and it can be concluded that using GND-RI as input features enables the classifier to learn more generalizable features than using only the original bands.

B. Spectral-Spatial Domain Classification

Remote sensing image classification corresponds to the semantic segmentation tasks of pixel-level classification in the field of computer vision. Mainstream semantic segmentation algorithms usually use an encoder-decoder architecture. The encoder part is a feature extraction network, which can be classified into convolutional networks [35] and ViT-like networks [36]. The decoder part is an upsampling network that upsamples the extracted high-level features to the original input resolution for pixel-level prediction [37]. Among the algorithms used in this study, ConvNeXt [38] and the Swin Transformer [39], which obtained SOTA results in the 2022 convolutional network and in the ViT, respectively, are chosen for the encoder part, and UPerNet [40], which is a unified perceptual resolution network for scene understanding, is used uniformly for the decoder part.

The selected image dataset is the RIT-18 dataset provided by Ronald Kemker [41], as shown in Fig. 9, which is an ultrahigh-resolution multispectral image from UAV imaging, with six spectral bands in the visible and near-infrared range and a spatial resolution of 0.047 m. Most importantly, the dataset contains two images of different illumination conditions at the same location, which is suitable for our test objectives.

Because the original RIT-18 dataset divides the features into 18 object categories with severely unbalanced class distributions, we reclassify the natural features and remove features, such as people, vehicles, and parking lines, so that the dataset only includes natural environment data. The specific categories and their corresponding sample sizes after reclassification are shown in Appendix A.

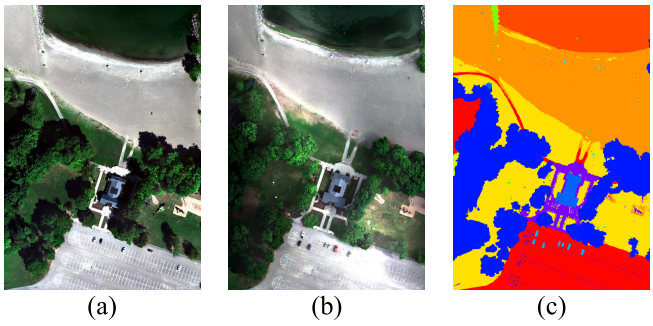

Fig. 9. RIT-18 dataset. (a) Image with shadows. (b) Image without shadows. (c) Label.

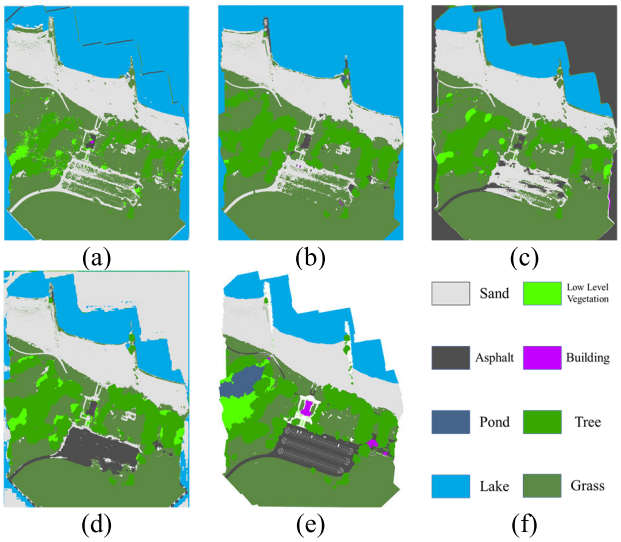

Fig. 10. Prediction results of the two experimental groups. (a) and (b) prediction results of ConvNeXt and the Swin Transformer for the feature band group. (c) and (d) prediction results of ConvNeXt and the Swin Transformer for the index group. (e) Label. (f) Legend.

As before, the experiments are also divided into the index group and the feature band group. Because of the lack of shortwave infrared bands used in the building index calculation, the index group only maps four of six bands used by the vegetation and water indices into the form of GND-RI, and the feature band group selects all six original bands as the input features. The specific experimental input features are shown in Table IV.

Since the algorithms in this section consider both spectral and texture features, it is difficult to explain the influence of GND-RI mapping on feature learning of classification models by comparing the classification results. The strategy of these experiments, therefore, is to use images without shadows [see Fig. 9(b)] for network training and images with shadows [see Fig. 9(a)] for validating the model accuracy, which illustrates the improvement of network generalization in the form of GND-RI in terms of the classification accuracy, including the mean intersection-over-union (mIoU) and all-pixel accuracy (aAcc). The accuracy validation results are shown in Table V, and the corresponding classification results are shown in Fig. 10.

From Table V, it can be seen that the accuracy for the index group is higher than that for the feature band group with both the ConvNeXt and Swin Transformer algorithms. More specifically, the mIoU for the index group is increased

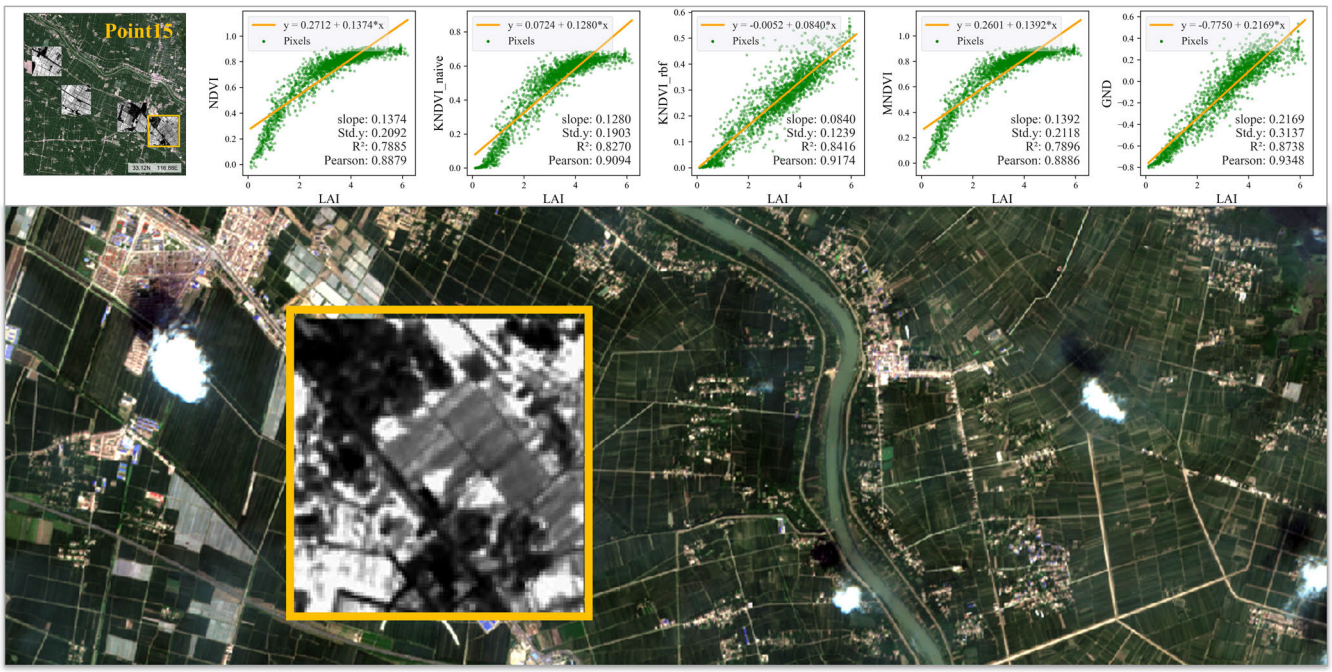

Fig. 11. Linear regression results of NDVI, KNDVI, MNDVI, and GND with LAI in Point15.

TABLE IV
INPUT FEATURES OF THE TWO EXPERIMENTAL GROUPS

Feature band group	Index group
	Water
○B2	● $NDWI = \frac{B2 - B5}{B2 + B5}$
○B5	● $RI_{water} = \sqrt{B2^2 + B5^2}$
	Vegetation
○B3	● $NDVI = \frac{B4 - B3}{B4 + B3}$
○B4	● $RI_{veg} = \sqrt{B4^2 + B3^2}$
○B1	●B1
○B6	●B6

TABLE V
OVERALL ACCURACY VALIDATION RESULTS OF THE TWO EXPERIMENTAL GROUPS

Backbone	Input	mIoU(%)	aAcc(%)
	RIT-18		
○Swin-T	band	38.20	46.42
○Swin-T	index	**52.06**(+13.86)	**58.48**(+12.06)
●ConvNeXt-T	band	36.55	45.36
●ConvNeXt-T	index	**39.48**(+2.93)	**47.78**(+2.42)

by 14.04%, and the aAcc is increased by 12.06% when the Swin Transformer is used as the backbone network compared with those for the feature group, and the mIoU for the index group is increased by 2.93%, and the aAcc is increased by 2.42% when ConvNeXt is used as the backbone network. From this, it can be concluded that GND-RI mapping enables the backbone networks to extract more generalizable features.

It is worth noting that the ConvNeXt and Swin Transformer networks used in this study have the same FLOPs, and ConvNeXt has higher classification accuracy with ImageNet-1K. In our experiments, mapping b_x and b_y to GND and RI, however, shows a significant improvement in the verification accuracy of the Swin Transformer, much more than that of ConvNeXt. We show the classification accuracies of ConvNeXt and Swin Transformer in detail in Appendix A, and based on this, we believe that a possible reason is that ConvNeXt may overfit the texture information with a small sample size.

V. DISCUSSION

First, the proposed GND and RI have achieved convincing results in remote sensing applications, but the prerequisites for their application mainly include the following two points.

1) The data source must be atmospherically corrected surface reflectance data.
2) The study target must possess a high contrast reflectance feature, and its data source also contains the corresponding feature band.

On the one hand, owing thanks to the improvement of satellite technology and the development of preprocessing techniques, multispectral surface reflectance data are easier to obtain, such as Sentinel-2 L2A data and Landsat 8/9 Collection 2 data, are easier to obtain. As shown in Fig. 11, GND can still achieve the best regression results after replacing the Landsat 8 satellite data in Section III with Sentinel L2A reflectance data. The Sentinel L2A data closest to the Landsat 8 data are only at Point 15.

The above data may have negative values or be greater than 1, and GND-RI mapping is bijective only in the half-plane

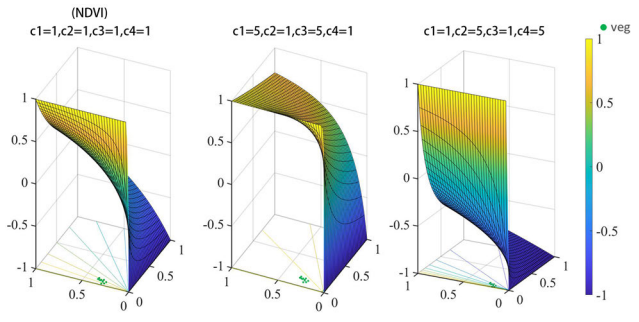

Fig. 12. 3-D function images and contour plots of GND for three groups with different scaling coefficients.

of the feature bands $b_x + b_y > 0$ or $b_x + b_y < 0$, so it is necessary to remove outliers before using GND-RI. After removal is completed, the value range of RI is fixed between 0 and $\sqrt{2}$.

Second, finding the high-contrast feature band corresponding to the study target in its data source is a challenge. For ground objects with unknown reflectance characteristics, spectral analysis is required to obtain the feature bands. For example, the study target and background objects are sampled, spectral profiles are plotted in the data source, and the feature bands are selected by manual comparison. In fact, traditional normalized difference indices often use this method for band selection.

When the data source is multi/hyperspectral data with a larger number of bands and a wider wavelength range, the manual band selection method is, however, no longer applicable. To solve this problem, we explored a machine learning-based band selection algorithm with the aim of replacing the manual selection of the feature bands applicable to GND. The principle of this algorithm is demonstrated in Appendix B.

Additionally, there are still some limitations to the GND approach of using scaling coefficients to change index sensitivity. Bounded functions will always face the problem of function saturation, and our aim is essentially to change the location of their relatively sensitive points. Fig. 12 shows the 3-D function images and contour maps corresponding to three different groups of GNDs with different scaling coefficients. It can be seen that the function of the scaling coefficients is actually to change the contour distribution of the indices at the specified location, and the denser the contour distribution is, the greater the gradient value and the more sensitive the index. For this reason, we recommend using the mean value of SR in the study area as the sensitive point of GND to derive the optimal coefficients for GND.

In summary, we contend that GND, with optimal coefficients, offers a more accurate representation of the superior inversion performance compared to the conventional NDI. We, therefore, recommend employing GND instead of NDI in works assessing index regression performance (e.g., the evaluation toolbox of the SI [26]).

VI. Conclusion

The functions of GND and RI in remote sensing applications can be summarized as follows.

TABLE VI
Individual Categories and the Corresponding Number of Pixels After Reclassification

Class	Pixel Count
Tree	6,065,240
Building	177,727
Low Level Vegetation	581,649
Grass	11,947,603
Lake	6,452,081
Pond	956,152
Asphalt	4,382,786
Sand	7,935,955

1) GND can be regarded as a function of SR, which serves as the only independent variable, and therefore, inherits the ability of SR to overcome illumination differences. As a result, GND exhibits robustness when applied to satellite imagery.
2) In change detection and variable inversion tasks, if the variable of interest induces changes in the ratio of feature bands (e.g., changes in vegetation coverage causing changes in RVI), using GND instead of NDI allows adaptive adjustment of the sensitivity of indices based on the characteristics of the study area, making it better suited to meet the application requirements. In this case, the ratio of coefficients c_4 and c_3 in GND should be set to the mean ratio value of feature bands b_y and b_x within the study area.
3) In machine learning classification algorithms based on spectral information, using GND-RI corresponding to the study targets instead of the original bands as the input features can suppress the influence of illumination differences, thus leading the classifier to learn more generalizable features.
4) For the deep learning classification algorithms based on the spectral-spatial domain, the usage of GND-RI corresponding to the study targets instead of the original bands as the input features achieves better classification accuracy. In particular, the improvement is larger for the ViT, with the mIoU improving by 14.04% and the aAcc improving by 12.06% in our experiments.

Finally, we need to cautiously state that the usage of GND and RI presupposes the existence of the high contrast feature bands of the targets in its data source. When the feature bands cannot be determined, it is recommended to use our band selection algorithm proposed in Appendix B for selection.

Appendix A

Table VI shows the specific categories and their corresponding sample sizes after reclassification.

Table VII shows the detailed classification results using ConvNeXt as the backbone network in the two groups of spectral-spatial domain experiments in Section IV. Except for low-level vegetation, higher accuracy is achieved with the index group. It is worth noting that asphalt is completely unidentifiable in the feature band group, while some accuracy is noted with the index group.

TABLE VII
CLASSIFICATION ACCURACY ON CONVNEXT

Class	IoU	Acc
	Index/ Band	
Tree	**53.84**/48.00	**66.32**/51.54
Building	0/0	0/0
Low Level Vegetation	9.92/**24.11**	11.23/**30.18**
Grass	**67.78**/58.34	95.15/**95.41**
Lake	**97.76**/94.75	**97.88**/95.16
Pond	0/0	0/0
Asphalt	**16.73**/0.33	**16.87**/0.33
Sand	**69.77**/64.84	**94.82**/90.27
aAcc	mIoU	mAcc
76.04/71.38	**39.48**/36.55	**47.78**/45.36

TABLE VIII
CLASSIFICATION ACCURACY ON SWIN TRANSFORMER

Class	IoU	Acc
	Index/ Band	
Tree	**71.59**/66.17	**88.09**/81.09
Building	0/0	0/0
Low Level Vegetation	**17.95**/1.48	**22.57**/1.48
Grass	**75.26**/64.99	92.93/**96.35**
Lake	**97.15**/96.61	**98.25**/96.68
Pond	0/0	0/0
Asphalt	**70.92**/1.82	**71.55**/1.84
Sand	**83.56**/74.56	**94.41**/93.95
aAcc	mIoU	mAcc
85.27/76.30	**52.06**/38.20	**58.48**/46.42

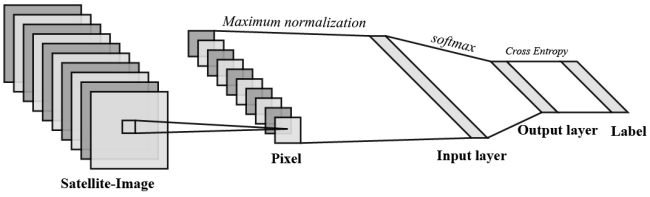

Fig. 13. Neural network architecture diagram.

Table VIII shows the detailed classification results using the Swin Transformer as the backbone network in the two groups of spectral-spatial domain experiments in Section IV. The accuracy for the index group is better than that of the feature band group in all aspects, and the recognition accuracies of the index values are higher than those for the feature band group in every accuracy category. Notably, asphalt in the feature band group is completely unrecognizable, while the IoU for the index group is as high as 70.92%.

APPENDIX B

To solve the problem of band selection of GND, we design a single-layer perceptron to perform band selection by analyzing the weights. Fig. 13 illustrates the network structure of the proposed perceptron.

The number of neurons in the input layer X is equal to the number of bands in the image N, where the jth neuron is denoted by X_j, and the value of X_j is the reflectance of band j after maximum normalization. The number of neurons in the output layer Z is equal to the number of categories in sample M, where the ith neuron is denoted by Z_i, and the value of Z_i is the value obtained by adding a bias term to the weighted sum of each neuron in the input layer and entering the softmax activation function. The loss is calculated between the output layer and the label using cross entropy. According to the chain derivation rule, the formula for calculating the negative gradient of each weight in the network proposed in this study is as follows:

$$-\nabla \text{loss} = -\frac{\partial \text{loss}}{\partial Z_i} \times \frac{\partial Z_i}{\partial Y_i} \times \frac{\partial Y_i}{\partial W_{ij}} = X_j(\overline{Z_i} - Z_i) \quad \text{(B1)}$$

where W_{ij} is the weight of the connection between the ith neuron in the output layer and the jth feature in the input layer and $\bar{Z}_i$ is the value of the ith row in the unique heat code. After training, the maximum weight $W_{\max}$ and the minimum weight $W_{\min}$ in the weight vector corresponding to neuron Z_i in the output layer are obtained. According to (B1), $W_{\max}$ connects the relatively larger X_j in the class i sample, and $W_{\min}$ connects the relatively larger X_j in the nonclass i sample. At this time, b_x connected by $W_{\max}$ and b_y connected by $W_{\min}$ can be used as the high-contrast feature bands required for the construction of GND in class i.

REFERENCES

[1] M. M. Verstraete and B. Pinty, "Designing optimal spectral indexes for remote sensing applications," *IEEE Trans. Geosci. Remote Sens.*, vol. 34, no. 5, pp. 1254–1265, Sep. 1996, doi: 10.1109/36.536541.

[2] J.-L. Widlowski, M. M. Verstraete, B. Pinty, and N. Gobron, "Advanced vegetation indices optimized for up-coming sensors: Design, performance, and applications," *IEEE Trans. Geosci. Remote Sens.*, vol. 38, no. 6, pp. 2489–2505, Nov. 2000, doi: 10.1109/36.885197.

[3] F. J. Kriegler, W. A. Malila, R. F. Nalepka, and W. Richardson, "Preprocessing transformations and their effects on multispectral recognition," in *Proc. 6th Int. Symp. Remote Sens. Environ.*, 1969, p. 97.

[4] J. Xue and B. Su, "Significant remote sensing vegetation indices: A review of developments and applications," *J. Sensors*, vol. 2017, May 2017, Art. no. 1353691, doi: 10.1155/2017/1353691.

[5] S. Huang, L. Tang, J. P. Hupy, Y. Wang, and G. Shao, "A commentary review on the use of Normalized Difference Vegetation Index (NDVI) in the era of popular remote sensing," *J. Forestry Res.*, vol. 32, no. 1, pp. 1–6, Feb. 2021, doi: 10.1007/s11676-020-01155-1.

[6] C. Unsalan and K. L. Boyer, "Classifying land development in high-resolution satellite imagery using hybrid structural-multispectral features," *IEEE Trans. Geosci. Remote Sens.*, vol. 42, no. 12, pp. 2840–2850, Dec. 2004, doi: 10.1109/TGRS.2004.835224.

[7] R. E. Kennedy, Z. Yang, and W. B. Cohen, "Detecting trends in forest disturbance and recovery using yearly Landsat time series: 1. LandTrendr—Temporal segmentation algorithms," *Remote Sens. Environ.*, vol. 114, no. 12, pp. 2897–2910, Dec. 2010, doi: 10.1016/j.rse.2010.07.008.

[8] D. Jia, C. Cheng, S. Shen, and L. Ning, "Multitask deep learning framework for spatiotemporal fusion of NDVI," *IEEE Trans. Geosci. Remote Sens.*, vol. 60, 2022, Art. no. 5616313, doi: 10.1109/TGRS.2021.3140144.

[9] R. B. Myneni, F. G. Hall, P. J. Sellers, and A. L. Marshak, "The interpretation of spectral vegetation indexes," *IEEE Trans. Geosci. Remote Sens.*, vol. 33, no. 2, pp. 481–486, Mar. 1995, doi: 10.1109/TGRS.1995.8746029.

[10] J. A. J. Berni, P. J. Zarco-Tejada, L. Suarez, and E. Fereres, "Thermal and narrowband multispectral remote sensing for vegetation monitoring from an unmanned aerial vehicle," *IEEE Trans. Geosci. Remote Sens.*, vol. 47, no. 3, pp. 722–738, Mar. 2009. [Online]. Available: http://ieeexplore.ieee.org

[11] M. J. L. García and V. Caselles, "Mapping burns and natural reforestation using thematic mapper data," *Geocarto Int.*, vol. 6, no. 1, pp. 31–37, Mar. 1991, doi: 10.1080/10106049109354290.

[12] J. D. Miller and A. E. Thode, "Quantifying burn severity in a heterogeneous landscape with a relative version of the delta Normalized Burn Ratio (dNBR)," *Remote Sens. Environ.*, vol. 109, no. 1, pp. 66–80, Jul. 2007, doi: 10.1016/j.rse.2006.12.006.

[13] S. K. McFeeters, "The use of the Normalized Difference Water Index (NDWI) in the delineation of open water features," *Int. J. Remote Sens.*, vol. 17, no. 7, pp. 1425–1432, May 1996, doi: 10.1080/01431169608948714.

[14] X. Han-Qiu, "A study on information extraction of water body with the modified normalized difference water index (MNDWI)," *Nat. Remote Sens. Bull.*, vol. 9, no. 5, pp. 589–595, 2005.

[15] Y. Zha, J. Gao, and S. Ni, "Use of normalized difference built-up index in automatically mapping urban areas from TM imagery," *Int. J. Remote Sens.*, vol. 24, no. 3, pp. 583–594, Jan. 2003, doi: 10.1080/01431160304987.

[16] D. K. Hall and G. A. Riggs, "Mapping global snow cover using Moderate Resolution Imaging Spectroradiometer (MODIS) data," *Glaciological Data*, vol. 4257, no. 95, pp. 13–17, 1995.

[17] B. Holben and C. Justice, "An examination of spectral band ratioing to reduce the topographic effect on remotely sensed data," *Int. J. Remote Sens.*, vol. 2, no. 2, pp. 115–133, Apr. 1981, doi: 10.1080/01431168108948349.

[18] W. Philpot, S. Jacquemoud, and J. Tian, "ND-space: Normalized difference spectral mapping," *Remote Sens. Environ.*, vol. 264, Oct. 2021, Art. no. 112622, doi: 10.1016/j.rse.2021.112622.

[19] C. Leprieur, M. M. Verstraete, and B. Pinty, "Evaluation of the performance of various vegetation indices to retrieve vegetation cover from AVHRR data," *Remote Sens. Rev.*, vol. 10, no. 4, pp. 265–284, Oct. 1994, doi: 10.1080/02757259409532250.

[20] A. Gonsamo and P. Pellikka, "The sensitivity based estimation of leaf area index from spectral vegetation indices," *ISPRS J. Photogramm. Remote Sens.*, vol. 70, pp. 15–25, Jun. 2012, doi: 10.1016/j.isprsjprs.2012.03.009.

[21] D. Vaiopoulos, G. A. Skianis, and K. Nikolakopoulos, "The contribution of probability theory in assessing the efficiency of two frequently used vegetation indices," *Int. J. Remote Sens.*, vol. 25, no. 20, pp. 4219–4236, Oct. 2004, doi: 10.1080/01431160410001680464.

[22] A. A. Gitelson, "Wide dynamic range vegetation index for remote quantification of biophysical characteristics of vegetation," *J. Plant Physiol.*, vol. 161, no. 2, pp. 165–173, Jan. 2004, doi: 10.1078/0176-1617-01176.

[23] G. Badgley, C. B. Field, and J. A. Berry, "Canopy near-infrared reflectance and terrestrial photosynthesis," *Sci. Adv.*, vol. 3, no. 3, pp. 1–6, Mar. 2017, doi: 10.1126/sciadv.1602244.

[24] G. Camps-Valls et al., "A unified vegetation index for quantifying the terrestrial biosphere," *Sci. Adv.*, vol. 7, no. 9, pp. 1–11, Feb. 2021, doi: 10.1126/sciadv.abc7447.

[25] B. Song, L. Liu, S. Du, X. Zhang, X. Chen, and H. Zhang, "ValLAI_Crop, a validation dataset for coarse-resolution satellite LAI products over Chinese cropland," *Sci. Data*, vol. 8, no. 1, pp. 1–16, Sep. 2021, doi: 10.1038/s41597-021-01024-4.

[26] J. Rivera, J. Verrelst, J. Delegido, F. Veroustraete, and J. Moreno, "On the semi-automatic retrieval of biophysical parameters based on spectral index optimization," *Remote Sens.*, vol. 6, no. 6, pp. 4927–4951, May 2014, doi: 10.3390/rs6064927.

[27] C. Cortes and V. Vapnik, "Support-vector networks," *Mach. Learn.*, vol. 20, no. 3, pp. 273–297, Sep. 1995, doi: 10.1007/BF00994018.

[28] S. S. Heydari and G. Mountrakis, "Effect of classifier selection, reference sample size, reference class distribution and scene heterogeneity in per-pixel classification accuracy using 26 Landsat sites," *Remote Sens. Environ.*, vol. 204, pp. 648–658, Jan. 2018, doi: 10.1016/j.rse.2017.09.035.

[29] L. Breiman, "Random forests," *Mach. Learn.*, vol. 45, no. 1, pp. 5–32, 2001, doi: 10.1023/A:1010933404324.

[30] V. F. Rodriguez-Galiano, M. Chica-Olmo, F. Abarca-Hernandez, P. M. Atkinson, and C. Jeganathan, "Random forest classification of Mediterranean land cover using multi-seasonal imagery and multi-seasonal texture," *Remote Sens. Environ.*, vol. 121, pp. 93–107, Jun. 2012, doi: 10.1016/j.rse.2011.12.003.

[31] J. Vrabel, "Multispectral imagery band sharpening study," *Photogramm. Eng. Remote Sens.*, vol. 62, no. 9, pp. 1075–1084, 1996.

[32] J. Vrabel, P. Doraiswamy, J. Mcmurtrey, and A. Stern, "Demonstration of the accuracy of improved-resolution hyperspectral imagery," *Proc. SPIE*, vol. 4725, pp. 556–567, Aug. 2002.

[33] D. Broomhead and D. Lowe, "Multivariable functional interpolation and adaptive networks," *Complex Syst.*, vol. 2, pp. 321–355, 1988.

[34] W. Wang, Z. Xu, W. Lu, and X. Zhang, "Determination of the spread parameter in the Gaussian kernel for classification and regression," *Neurocomputing*, vol. 55, nos. 3–4, pp. 643–663, 2003, doi: 10.1016/S0925-2312(02)00632-X.

[35] E. Shelhamer, J. Long, and T. Darrell, "Fully convolutional networks for semantic segmentation," *IEEE Trans. Pattern Anal. Mach. Intell.*, vol. 39, no. 4, pp. 640–651, Apr. 2017, doi: 10.1109/TPAMI.2016.2572683.

[36] A. Dosovitskiy et al., "An image is worth 16 × 16 words: Transformers for image recognition at scale," 2020, *arXiv:2010.11929*.

[37] MMS. Contributors. (2020). *MMSegmentation: OpenMMLab Semantic Segmentation Toolbox and Benchmark*. [Online]. Available: https://github.com/open-mmlab/mmsegmentation

[38] Z. Liu, H. Mao, C.-Y. Wu, C. Feichtenhofer, T. Darrell, and S. Xie, "A ConvNet for the 2020s," in *Proc. IEEE/CVF Conf. Comput. Vis. Pattern Recognit. (CVPR)*, Jun. 2022, pp. 11966–11976.

[39] Z. Liu et al., "Swin Transformer: Hierarchical vision transformer using shifted windows," in *Proc. IEEE/CVF Int. Conf. Comput. Vis. (ICCV)*, Oct. 2021, pp. 10012–10022, doi: 10.1109/ICCV48922.2021.00986.

[40] T. Xiao, Y. Liu, B. Zhou, Y. Jiang, and J. Sun, "Unified perceptual parsing for scene understanding," in *Proc. Eur. Conf. Comput. Vis. (ECCV)*, 2018, pp. 418–434.

[41] R. Kemker, C. Salvaggio, and C. Kanan, "Algorithms for semantic segmentation of multispectral remote sensing imagery using deep learning," *ISPRS J. Photogramm. Remote Sens.*, vol. 145, pp. 60–77, Nov. 2018, doi: 10.1016/j.isprsjprs.2018.04.014.

Linxin Zou received the B.S. and M.Sc. degree from the Guilin University of Technology, Guilin, China, in 2019 and 2022, respectively.

He is currently a member of the Guangxi Key Laboratory of Spatial Information and Geomatics, Guilin University of Technology. His research interests include explainable and physics-aware artificial intelligence, radiation transfer models, satellite image processing, and open-source deep learning frameworks. He is currently developing remote sensing applications based on OpenMMLab and is a contributor to MMsegmentation.

Bo Wei received the Ph.D. degree in geoinformation engineering from the School of Land Science and Technology, China University of Geosciences (Beijing), Beijing, China, in 2012.

He is currently a Professor with the College of Geomatics and Geoinformation, Guilin University of Technology, Guilin, China. His research interests include temporal–spatial data analysis, machine learning, and remote sensing image processing.